Modeling breast ultrasound; on the applicability of commonly made approximations

Taskin, Ulas; Ozmen, Neslihan; Gemmeke, Hartmut; Van Dongen, Koen W.A.

DOI
10.24425/123914

Publication date
2018

Document Version
Final published version

Published in
Archives of Acoustics

Citation (APA)
Taskin, U., Ozmen, N., Gemmeke, H., & Van Dongen, K. W. A. (2018). Modeling breast ultrasound; on the applicability of commonly made approximations. *Archives of Acoustics*, *43*(3), 425-435. https://doi.org/10.24425/123914

www.czasopisma.pan.pl PAN POLSKA AKADEMIA NAUK www.journals.pan.pl

PAN ARCHIVES OF ACOUSTICS
Vol. **43**, No. 3, pp. 425–435 (2018)

DOI: 10.24425/123914

Modeling Breast Ultrasound; on the Applicability of Commonly Made Approximations

Ulas TASKIN[(1)], Neslihan OZMEN[(2)], Hartmut GEMMEKE[(3)], Koen W.A. van DONGEN[(1)]

[(1)] *Laboratory of Acoustical Wavefield Imaging*
Faculty of Applied Sciences
Delft University of Technology
2600 GA Delft, The Netherlands; e-mail: u.taskin@tudelft.nl

[(2)] *Philips Healthcare*
5684 PC Best, The Netherlands

[(3)] *KIT, Institute for Electronics and Data Processing*
76021 Karlsruhe, Germany

(*received November 15, 2017; accepted April 16, 2018*)

To design breast ultrasound scanning systems or to test new imaging methods, various computer models are used to simulate the acoustic wave field propagation through a breast. The computer models vary in complexity depending on the applied approximations. The objective of this paper is to investigate how the applied approximations affect the resulting wave field. In particular, we investigate the importance of taking three-dimensional (3-D) spatial variations in the compressibility, volume density of mass, and attenuation into account. In addition, we compare four 3-D solution methods: a full-wave method, a Born approximation method, a parabolic approximation method, and a ray-based method. Results show that, for frequencies below 1 MHz, the amplitude of the fields scattering off the compressibility or density contrasts are at least 24 dB higher than the amplitude of the fields scattering off the attenuation contrasts. The results also show that considering only speed of sound as a contrast is a valid approximation. In addition, it is shown that the pressure field modeled with the full-wave method is more accurate than the fields modeled using the other three methods. Finally, the accuracy of the full-wave method is location independent whereas the accuracy of the other methods strongly depends on the point of observation.

Keywords: breast ultrasound; forward modeling; full-wave method.

1. Introduction

Breast cancer is the most frequently diagnosed type of cancer and among the leading causes of death for women worldwide. Several studies show that detecting the tumor at an early stage significantly increases the survival rate (Siegel *et al.*, 2017). Currently, X-ray mammography is generally used in screening programs since it is the "golden standard" for breast cancer examination. However, it can miss tumors in young women with dense breasts as the healthy fibrous and glandular tissues, as well as cancerous lumps, show up white on mammograms (Bird *et al.*, 1992). Fortunately, ultrasound has the capability to differentiate between these tissues and therefore it has the potential to detect cancer in dense breasts. In addition, it is patient-friendly, safe, fast, cost-effective and avoids the use of ionizing radiation. To improve breast cancer diagnosis, automated whole-breast ultrasound scanning systems (Ruiter *et al.*, 2006; Wiskin *et al.*, 2012; Duric *et al.*, 2007) and ultrasound imaging algorithms (Simonetti *et al.*, 2007; Hesse, Schmitz, 2012; Jirik *et al.*, 2012; Ozmen *et al.*, 2015) are being developed.

To optimize the design of a breast scanner, it is essential to model the acoustic wave field generated by the system. In addition, to test new imaging methods, computer models can be used as an appropriate, inexpensive, and flexible approach for generating synthetic measurement data. However, for these models to be useful, it is important to know (i) what the relevant medium parameters are and (ii) the applicability of approximations commonly made to reduce the compu-

tational costs involved in solving the forward problem. It is the objective of this paper to investigate those two aspects.

To investigate what the relevant medium parameters are, we model the pressure field using a three-dimensional (3-D) full-wave method. The applied method uses a frequency-domain integral equation formulation to describe the wave propagation in media with spatially varying compressibility, volume density of mass and attenuation (van Dongen, Wright, 2006; Ozmen-Eryilmaz *et al.*, 2011). The applied numerical breast model is built from an MRI scan of cancerous breast (Bakker *et al.*, 2009). Time-domain results are obtained by applying Fourier transformations. The method accounts for refraction, diffraction, multiple reflections, and/or dispersion effects.

The same full-wave method is used to examine the performance of commonly used approximations to solve the forward problem in biomedical ultrasound. In particular, we will evaluate the Born approximation (Simonetti *et al.*, 2007), paraxial approximation (Hardin, Tappert, 1973) and ray based method (Kak, Slaney, 1988). The effects of these approximations are studied by comparing the resulting wave fields with the solutions obtained with the full-wave method. We used the basic form of each approximation instead of recent methods based on these approximations that can give more accurate results. The main reason behind this selection is to point out possible problems each approximation may bring.

The integral equation formulation (Cobbold, 2007) has the advantage that it allows the problem to be solved at a predefined accuracy using an iterative solution method (Herman, van den Berg, 1982). In this work a conjugate gradient iterative solution method is used (Kleinman, van den Berg, 1991). An additional advantage of the frequency-domain formulation is that it leads to a reduction of computational complexity. This is especially the case, if one is only interested in the dominant spectral component of the temporal signal. Since each frequency component may be considered as an independent problem, parallelization techniques can be used to reduce the computational time.

To investigate the aforementioned aspects, we start Sec. 2 with introducing the integral equation formulation for the acoustic wave field. Section 3 provides details about four different solution methods: full-wave method, Born approximation, paraxial approximation and ray based method. Section 4 first validates the accuracy of the full-wave method using the analytical solution for a plane wave scattering off a spherical contrast. Next, it evaluates how the different medium properties affect the pressure wave field and ends with comparing the time-domain results obtained with the four solution methods. Finally, Sec. 5 contains a discussion of the obtained results and a final conclusion.

2. Theory

The propagation of acoustic pressure wave fields in heterogeneous media is governed by the wave equation. Derivation of this wave equation starts with the equations of motion and deformation. In the frequency domain these equations equal

$$\nabla\widehat{p}(\mathbf{x}) + i\omega\rho(\mathbf{x})\widehat{\mathbf{v}}(\mathbf{x}) = \widehat{\mathbf{f}}(\mathbf{x}), \tag{1}$$

$$\nabla\cdot\widehat{\mathbf{v}}(\mathbf{x}) + i\omega\kappa(\mathbf{x})\widehat{m}(\mathbf{x})\widehat{p}(\mathbf{x}) = \widehat{q}(\mathbf{x}), \tag{2}$$

where $\widehat{p}(\mathbf{x})$ is the acoustic pressure wave field, $\widehat{\mathbf{v}}(\mathbf{x})$ is the particle velocity wave field, $\rho(\mathbf{x})$ is the volume density of mass, $\kappa(\mathbf{x})$ is the compressibility, $\widehat{m}(\mathbf{x})$ is the causal compliance relaxation function to account for attenuation, $\widehat{\mathbf{f}}(\mathbf{x})$ is the volume source density of volume force, and $\widehat{q}(\mathbf{x})$ is the volume source density of injection rate, ∇ is the nabla operator, ω is the angular frequency, and $\mathbf{x}$ is the spatial coordinate in the 3-D spatial domain $\mathbb{D}$ (Fokkema, van den Berg, 1993; Gisolf, Verschuur, 2010; Demi *et al.*, 2011; Huijssen *et al.*, 2008). The caret symbol $\widehat{\ }$ is used to express that a quantity is defined in the temporal Fourier domain. Combining Eqs. (1) and (2) results in the inhomogeneous Helmholtz equation for heterogeneous media, i.e.

$$\nabla^2\widehat{p}(\mathbf{x}) - \widehat{\gamma}_0^2\widehat{p}(\mathbf{x}) = -i\omega\rho(\mathbf{x})\widehat{q}(\mathbf{x}) + \chi_\rho(\mathbf{x})\nabla\widehat{p}(\mathbf{x}) - \widehat{\chi}_\gamma(\mathbf{x})\widehat{p}(\mathbf{x}), \tag{3}$$

where $\nabla^2 = \nabla\cdot\nabla$ is the Laplace operator, $\gamma_0 = i\omega\sqrt{\rho_0\kappa_0 m_0}$ is the propagation coefficient of the embedding, and $\chi_\rho(\mathbf{x})$ and $\widehat{\chi}_\gamma(\mathbf{x})$ are contrast functions. These contrast functions depend on the spatially varying medium properties compressibility, density and attenuation, and are equal to

$$\chi_\rho(\mathbf{x}) = \frac{\nabla\rho(\mathbf{x})}{\rho(\mathbf{x})} \tag{4}$$

and

$$\widehat{\chi}_\gamma(\mathbf{x}) = \widehat{\gamma}_0^2 - \widehat{\gamma}^2(\mathbf{x}). \tag{5}$$

In Eqs. (3) to (5) it is assumed that the wave fields are solely generated by a volume source density of injection rate source $\widehat{q}(\mathbf{x})$, hence $\widehat{\mathbf{f}}(\mathbf{x}) = 0$. In addition, it is assumed that both the volume density of mass $\rho(\mathbf{x})$ and the velocity wave field $\widehat{\mathbf{v}}(\mathbf{x})$ are sufficiently smooth. These assumptions are typically valid for most biomedical applications.

To account for the power law attenuation commonly observed in biomedical tissue, the complex propagation coefficient $\widehat{\gamma}(\mathbf{x})$ is expressed as

$$\widehat{\gamma}(\mathbf{x}) = \widehat{\alpha}(\mathbf{x}) + i\widehat{\beta}(\mathbf{x}), \tag{6}$$

where the attenuation coefficient $\widehat{\alpha}(\mathbf{x})$ and phase coefficient $\widehat{\beta}(\mathbf{x})$ equal (Szabo, 1995)

$$\widehat{\alpha}(\mathbf{x}) = \alpha_1(\mathbf{x})\,|\omega|^{b(\mathbf{x})}, \tag{7}$$

$$\widehat{\beta}(\mathbf{x}) = \frac{\omega}{c_{\text{ref}}} + \alpha_1(\mathbf{x})\tan\left[\frac{\pi}{2}b(\mathbf{x})\right] \cdot\omega(|\omega|^{b(\mathbf{x})-1} - |\omega_{\text{ref}}|^{b(\mathbf{x})-1}), \tag{8}$$

with

$$\alpha_1(\mathbf{x}) = a(\mathbf{x})(2\pi)^{-b(\mathbf{x})}, \tag{9}$$

where ω_{ref} is the angular reference frequency at which the speed of sound and attenuation coefficients have been measured and the medium parameters $a(\mathbf{x})$ and $b(\mathbf{x})$ reflect the attenuation.

Equation (3) can be recasted into an integral equation which equals

$$\widehat{p}(\mathbf{x}) = \widehat{p}_{\text{inc}}(\mathbf{x}) + \int_{\mathbf{x}'\in\mathbb{D}} \widehat{G}(\mathbf{x}-\mathbf{x}')\chi_\rho(\mathbf{x}')\nabla\widehat{p}(\mathbf{x})\,\mathrm{d}V + \int_{\mathbf{x}'\in\mathbb{D}} \widehat{G}(\mathbf{x}-\mathbf{x}')\widehat{\chi}_\gamma(\mathbf{x}')\widehat{p}(\mathbf{x}')\,\mathrm{d}V, \tag{10}$$

where $\widehat{p}_{\text{inc}}(\mathbf{x})$ is referred to as the incident field, i.e., the pressure wave field generated by the primary sources and propagating in the homogeneous embedding and where $\widehat{G}(\mathbf{x}-\mathbf{x}')$ is the free-space Green's function of the homogeneous embedding. This function satisfies the Sommerfeld radiation condition and the application of the absorbing boundary conditions or perfectly matched layers are not needed as long as the contrast is embedded in the background medium (Alles, van Dongen, 2011). For the 3-D case the free-space Green's function of homogeneous background equals

$$\widehat{G}(\mathbf{x}-\mathbf{x}') = \frac{\mathrm{e}^{-\gamma_0|\mathbf{x}-\mathbf{x}'|}}{4\pi\,|\mathbf{x}-\mathbf{x}'|}. \tag{11}$$

In the remaining of the paper, when it is mentioned that there is only a compressibility contrast it means that both the density and attenuation is constant and set to values corresponding to the embedding, hence, $\rho(\mathbf{x}) = \rho_0$, $a(\mathbf{x}) = a_0$ and $b(\mathbf{x}) = b_0$. The same procedure is followed in case that there is only a density or an attenuation contrast. For the case that all inhomogeneities are combined, every parameter has its actual value. The speed of sound case is an approximation that is commonly made. In this case attenuation is set to the embedding, and the contrast function χ_ρ given in Eq. (4) is set to 0. Only the contrast function χ_γ is non-zero where the speed of sound is based on the actual values of the compressibility and density.

3. Solution methods

The forward problem refers to the situation where the unknown total pressure field $\widehat{p}(\mathbf{x})$ is obtained for a known incident pressure field $\widehat{p}_{\text{inc}}(\mathbf{x})$ and known contrast functions $\chi_\rho(\mathbf{x}')$ and $\widehat{\chi}_\gamma(\mathbf{x}')$. Solving the forward problem via Eq. (10) requires the use of iterative schemes in situations when arbitrary shaped contrasts are considered; exact analytical solutions only exist for a limited number of configurations. In addition to the full-wave method, we also derive solution methods for the Born approximation, the paraxial approximation, and the ray based method.

3.1. Full-wave method

The presented full-wave method is based on the frequency-domain integral equation formulation as presented in Eq. (10) (van Dongen, Wright, 2006; Ozmen-Eryilmaz *et al.*, 2011). This equation can be rewritten as

$$\widehat{p}_{\text{inc}}(\mathbf{x}) = \widehat{p}(\mathbf{x}) - \int_{\mathbf{x}'\in\mathbb{D}} \widehat{G}(\mathbf{x}-\mathbf{x}')\chi_\rho(\mathbf{x}')\nabla\widehat{p}(\mathbf{x})\,\mathrm{d}V - \int_{\mathbf{x}'\in\mathbb{D}} \widehat{G}(\mathbf{x}-\mathbf{x}')\widehat{\chi}_\gamma(\mathbf{x}')\widehat{p}(\mathbf{x}')\,\mathrm{d}V. \tag{12}$$

In operator notation Eq. (12) equals

$$\mathsf{f} = \mathsf{L}[\mathsf{u}], \tag{13}$$

where f is the known incident pressure field $\widehat{p}_{\text{inc}}(\boldsymbol{x})$, u is the unknown total pressure field $\widehat{p}(\boldsymbol{x})$, and L is the integral operator containing the Green's function $\widehat{G}(\boldsymbol{x}-\boldsymbol{x}')$, and the known contrast functions $\chi_\rho(\boldsymbol{x}')$ and $\widehat{\chi}_\gamma(\boldsymbol{x}')$. In our study, the linear system is solved iteratively by the conjugate gradient method applied on the normal equation. The convergence of this method is known to be good (va Dongen *et al.*, 2007). With this method the unknown field at the n-th iteration step, i.e. u_n, is obtained by minimizing a cost functional. Hence, the approximate solution at the n-th iteration step equals

$$\mathsf{u}_\mathsf{n} = \mathsf{u}_{\mathsf{n}-1} + \alpha_\mathsf{n}\mathsf{d}_\mathsf{n}, \qquad \mathsf{n} \geq 1, \tag{14}$$

where α_n is the step size and d_n is the update direction. Step size is determined according to the Fletcher-Reeves formula (Fletcher, 1976). For any updated solution u_n the residual r_n is defined as

$$\mathsf{r}_\mathsf{n} = \mathsf{f} - \mathsf{L}[\mathsf{u}_\mathsf{n}], \tag{15}$$

and the normalized error Err_n is defined as

$$\mathsf{Err}_\mathsf{n} = \frac{\|\mathsf{r}_\mathsf{n}\|}{\|\mathsf{f}\|}, \tag{16}$$

with the properties $\mathsf{Err}_\mathsf{n} = 0$ if $\mathsf{u}_\mathsf{n} = \mathsf{u}$, and $\mathsf{Err}_\mathsf{n} = 1$ if $\mathsf{u}_\mathsf{n} = 0$, and where $\|\ldots\|^2$ represents the L_2-norm of a vector. The error is used as a measure for the accuracy attained in the iterative scheme. All detailed steps of the conjugate gradient method are given in Table 1. Note that problems associated with the singularity of the Green's function are solved by using its weak form (Zwamborn, van den Berg, 1992).

Table 1. The conjugate gradient scheme ($\mathsf{L}^\dagger$ is the adjoint operator).

CG
$\mathsf{u}_0 = 0$
$\mathsf{r}_0 = \mathsf{f} - \mathsf{L}[\mathsf{u}_0]$
$\mathsf{d}_0 = \mathsf{r}_0$
$\mathsf{g}_0 = \mathsf{L}^\dagger[\mathsf{r}_0]$
for $n = 1, 2, ...$
$\mathsf{g}_n = \mathsf{L}^\dagger[\mathsf{r}_{n-1}]$
$\eta_n = \dfrac{\|\mathsf{g}_n\|^2}{\|\mathsf{g}_{n-1}\|^2}$
$\mathsf{d}_n = \mathsf{g}_n + \eta_n \mathsf{d}_{n-1}$
$\alpha_n = \dfrac{\|\mathsf{g}_n\|^2}{\|\mathsf{L}\mathsf{d}_n\|^2}$
$\mathsf{u}_n = \mathsf{u}_{n-1} + \alpha_n \mathsf{d}_n$
$\mathsf{r}_n = \mathsf{f} - \mathsf{L}[\mathsf{u}_n]$
$\mathsf{Err}_n = \dfrac{\|\mathsf{r}_n\|}{\|\mathsf{f}\|}$
if $\mathsf{Err}_n < \epsilon$ stop
if $\mathsf{n} > \mathsf{n}_{\max}$ stop
end

3.2. Born approximation

In situations where the contrasts are small and the scattering is weak, the unknown total field $\widehat{p}(\mathbf{x})$, inside the integrand of Eq. (10) may be approximated by the known incident field $\widehat{p}_{\text{inc}}(\mathbf{x})$, yielding the following equation

$$\widehat{p}(\mathbf{x}) = \widehat{p}_{\text{inc}}(\mathbf{x}) + \int\limits_{\mathbf{x}'\in\mathbb{D}} \widehat{G}(\mathbf{x}-\mathbf{x}')\chi_\rho(\mathbf{x}')\nabla\widehat{p}_{\text{inc}}(\mathbf{x}')\,\mathrm{d}V + \int\limits_{\mathbf{x}'\in\mathbb{D}} \widehat{G}(\mathbf{x}-\mathbf{x}')\widehat{\chi}_\gamma(\mathbf{x}')\widehat{p}_{\text{inc}}(\mathbf{x}')\,\mathrm{d}V. \tag{17}$$

The unknown total field can now be computed directly and is similar to the field obtained after the first iteration step of the conjugate gradient solution method. Although this approximation neglects multiple scattering and possible phase shifts in the resulting field, it is highly efficient with respect to computational time.

3.3. Paraxial approximation

To solve the wave equation within the paraxial approximation, the parabolic wave equation is used as a starting point (Dagrau *et al.*, 2011). Under the assumption that spatial variations depend on speed of sound, the Helmholtz equation reads

$$\nabla^2\widehat{p}(\mathbf{x}) + \widehat{k}^2(\mathbf{x})\widehat{p}(\mathbf{x}) = 0, \tag{18}$$

where the wave number $\widehat{k}(\mathbf{x})$ equals

$$\widehat{k}(\mathbf{x}) = \frac{\omega}{c(\mathbf{x})}, \tag{19}$$

and where $c(\mathbf{x})$ is the speed of sound of the medium. After applying a spatial Fourier transform with respect to x and y Eq. (18) equals

$$\frac{\partial\widetilde{p}}{\partial z^2} + \left(\widetilde{k^2} *_{k_x,k_y} -k_x^2 - k_y^2\right)\widetilde{p} = 0, \tag{20}$$

where the tilde symbol $\widetilde{\ }$ is used to express that a quantity is defined in the spatial Fourier domain (k_x, k_y) with Cartesian coordinate z, and where the symbol $*_{k_x,k_y}$ denotes a convolution with respect to the spatial frequency components (k_x, k_y). Equation (20) can be factorized into two parts, i.e.

$$\left[\frac{\partial}{\partial z} - i\,\widetilde{k}_z\right]\left[\frac{\partial}{\partial z} + i\,\widetilde{k}_z\right]\widetilde{p} = 0, \tag{21}$$

with

$$\widetilde{k}_z = \sqrt{\widetilde{k^2} *_{k_x,k_y} -k_x^2 - k_y^2}. \tag{22}$$

To compute the wave propagating in the $+z$-direction, only the second part of the left-hand side of Eq. (21) is considered, hence

$$\left[\frac{\partial}{\partial z} + i\widetilde{k}_z\right]\widetilde{p} = 0. \tag{23}$$

A solution for the one-way wave equation (Eq. (23)) is obtained using the split-step method (Stoffa *et al.*, 1990). Using the known field in the plane $z = z_0$, the field at $z = z_o + \Delta$ can be computed in following way

$$\widetilde{p}(k_x, k_y, z_0 + \Delta) = \widetilde{p}(k_x, k_y, z_0)\mathrm{e}^{-i\widetilde{k}_z\Delta}, \tag{24}$$

where $\widetilde{k}_z$ is approximated as

$$\widetilde{k}_z = \widehat{k}_{\text{mean}} + \frac{(k_x^2 + k_y^2)}{2\widehat{k}_{\text{mean}}}, \tag{25}$$

with

$$\widehat{k}_{\text{mean}} = \frac{\displaystyle\int \widehat{k}(x, y, z)\,\mathrm{d}x\,\mathrm{d}y}{\displaystyle\int \mathrm{d}x\,\mathrm{d}y}. \tag{26}$$

This approximation is only valid when the angle between the z-axis and the direction of propagation is small. Note that there are several methods to approximate $\widetilde{k}_z$, all leading to similar results.

3.4. Ray based method

The ray based method assumes that the pressure field travels along a straight path and spatial variations in the speed of sound only lead to phase shifts. Solutions for the forward problem are constructed by calculating the phase shifts for every point in the domain of interest (Kak, Slaney, 1988).

4. Results

Numerical results are provided in this section in the following order. First, the full-wave method is validated using an analytical solution for a plane wave scattering off a spherical object. Next, several simulations are presented using a breast model with inhomogeneities in all four medium properties separately and combined. Finally, a comparison is made of the results obtained with different solution methods in case only inhomogeneities in the speed of sound are considered. All fields are on a dB scale and normalized with respect to the maximum absolute value of the incident field unless noted otherwise.

4.1. Validation with an analytical solution

To test the accuracy of the full-wave method, a configuration is used for which the analytical solution is known: a plane wave scattering off a spherical object. A derivation of the analytical solution can be found in the literature (Skudrzyk, 2012). The acoustically penetrable sphere with radius $r = 2.5$ mm is positioned in the center of a volume of $10 \times 10 \times 10$ mm. The spatial domain is discretized with a grid size $\Delta x = 0.078$ mm in each direction. The acoustic medium parameters of the sphere and the embedding are chosen similar to those typically encountered in biomedical applications. It is considered that the sphere represents fat and the embedding represents water, see Table 2. The sphere is illuminated with a plane wave propagating in the x-direction. The Gaussian modulated wave has a center frequency $f_0 = 1$ MHz, and a bandwidth of 50%. The time span of the simulation is set to 16 μs with a step size $\Delta t = 0.25$ μs. The iterative scheme is stopped when the normalized error is $\mathsf{Err}_n \leq 10^{-6}$. Time-domain results are obtained by applying inverse Fourier transforms.

Table 2. Acoustic medium parameters for the breast (Szabo, 2004; Goss *et al.*, 1980; d'Astous, Foster, 1986; Duck, 2013; Sohrab *et al.*, 2006).

	c [m/s]	ρ [kg/m^3]	κ [1/Pa]	a [dB/mMHz^b]	b [–]
Water**	1510	995	4.41e−10	0.2	2.00
Muscle	1580	1041	3.85e−10	57.0	1.01*
Fat	1430	928	5.27e−10	15.8	1.70
Skin	1537	1200	3.53e−10	104.0	1.01*
Gland	1510	1020	4.30e−10	75.0	1.50
Tumor	1550	1000	4.16e−10	57.0	1.30

* Assumed values, ** at a temperature of 32°C.

Snapshots of the incident, total and scattered fields at time $t = 4.75$ μs in the plane $z = 0$ m are presented in Fig. 1. The normalized error between the analytical solution $p_{\mathrm{AS}}(\mathbf{x}, t)$ and full-wave method $p_{\mathrm{FW}}(\mathbf{x}, t)$ is calculated for the incident, total and scattered field, as

$$\mathsf{Error}(\mathbf{x}, t) = 20 \log_{10} \left(\frac{|p_{\mathrm{FW}}(\mathbf{x}, t) - p_{\mathrm{AS}}(\mathbf{x}, t)|}{|p_{\mathrm{AS}}(\mathbf{x}, t)|} \right), \quad (27)$$

where $|\ldots|$ indicates that the absolute value is taken. As can be seen in Fig. 1, the differences between both solutions are small, i.e. everywhere below −40 dB. For instance, the normalized error in the total field near the

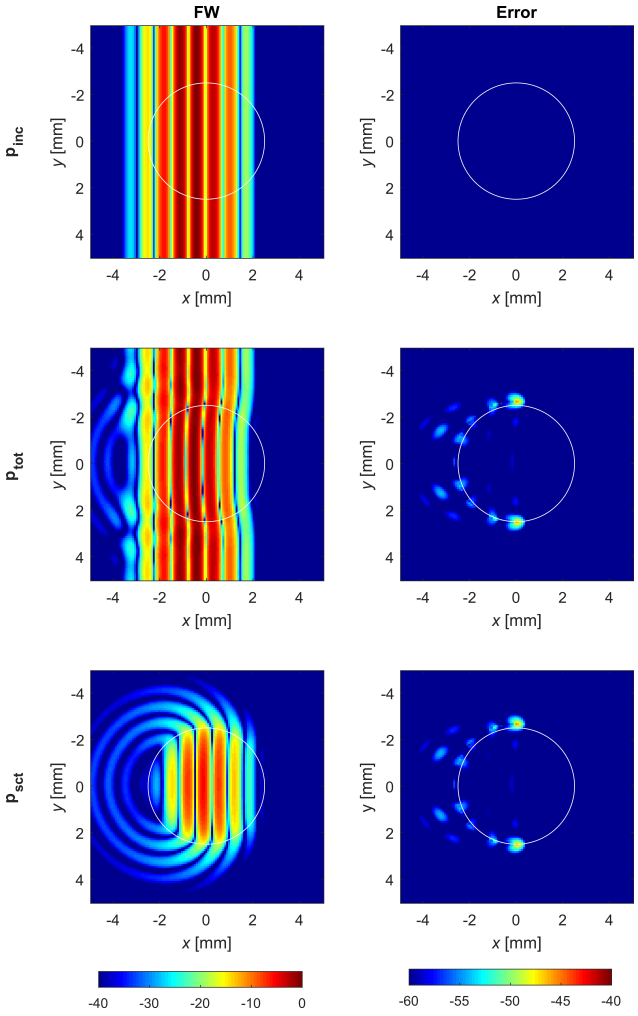

Fig. 1. Snapshots of the incident (top row), total (middle row) and scattered (bottom row) pressure fields in dB at time $t = 4.75$ μs, and in the plane $z = 0$ m. The first column shows the full-wave method, and the second column shows the error between the analytical and the full-wave solution. The white circle shows the contour of the sphere which is located in the middle of the domain.

border of the sphere is around −45 dB and is mainly due to the spatial discretization of the sphere.

4.2. Investigating the effect of different inhomogeneities

The presented full-wave method is used to investigate the effect of the different acoustic medium properties. For this study, a breast model built from an MRI scan of a real cancerous breast is used (see Fig. 2) (Bakker *et al.*, 2009). The breast model is submerged in water and has acoustic medium parameters as shown in Table 2.

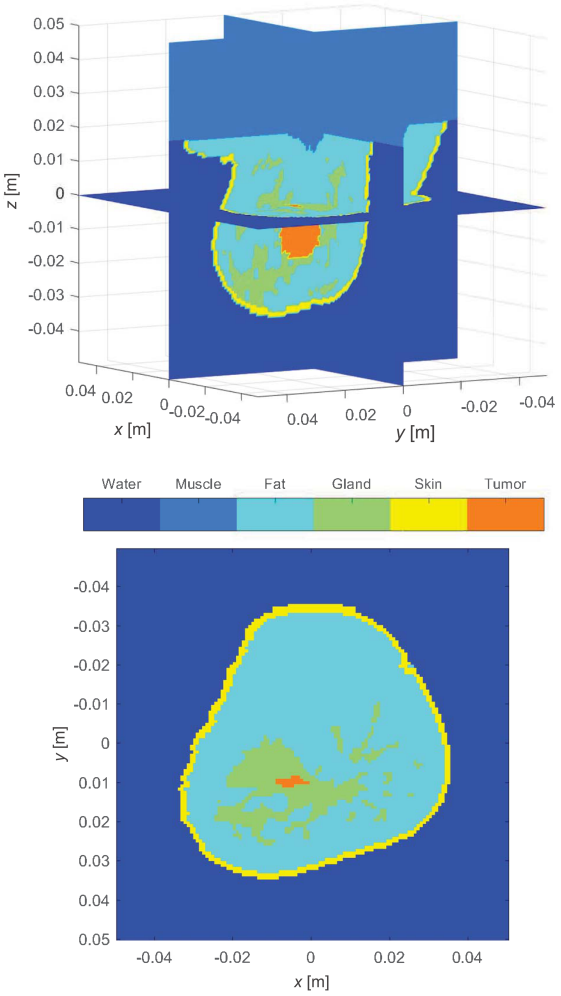

Fig. 2. Tissue types for the 3-D breast model built from an MRI scan of a cancerous breast (Bakker *et al.*, 2009). The bottom image displays a cross-section of the breast at $z = 0$ m. The wave fields presented in Fig. 3 to 6 are taken in this cross-sectional plane.

For the simulations, the time span considered equals 128 µs, and is discretized with a time step $\Delta t = 1$ µs. A point source, located in the point $(x_s, y_s, z_s) = (0\text{ m}, -0.05\text{ m}, 0\text{ m})$, generates a Gaussian modulated field with center frequency $f_0 = 0.25$ MHz and 50% bandwidth. The spatial domain equals $0.1 \times 0.1 \times 0.1$ m and is discretized with a uniform grid size $\Delta x = 0.78$ mm. The stopping criterion is set to $\mathsf{Err}_n \leq 10^{-6}$.

To investigate the effect of each acoustic medium property separately, the forward problem is solved five times; one simulation where all medium properties are set to their appropriate values, and four simulations where only one of the four medium properties has its appropriate value and where the remaining properties are set to values corresponding to the embedding (i.e. water). Figure 3 shows the scattered pressure fields in the plane $z = 0$ m evaluated at four different frequencies (0.125 MHz, 0.25 MHz, 0.5 MHz and 1 MHz) and for the four medium properties separately and combined. The scattering caused by the different inhomogeneities are clearly visible. The images show that the amount of scattering increases for increasing frequency. In addition, it is shown that for these frequencies the amount of scattering caused by inhomogeneities in the compressibility and density is significantly larger than the scattering caused by inhomogeneities in the attenuation. Maximum values of the fields displayed in Fig. 3

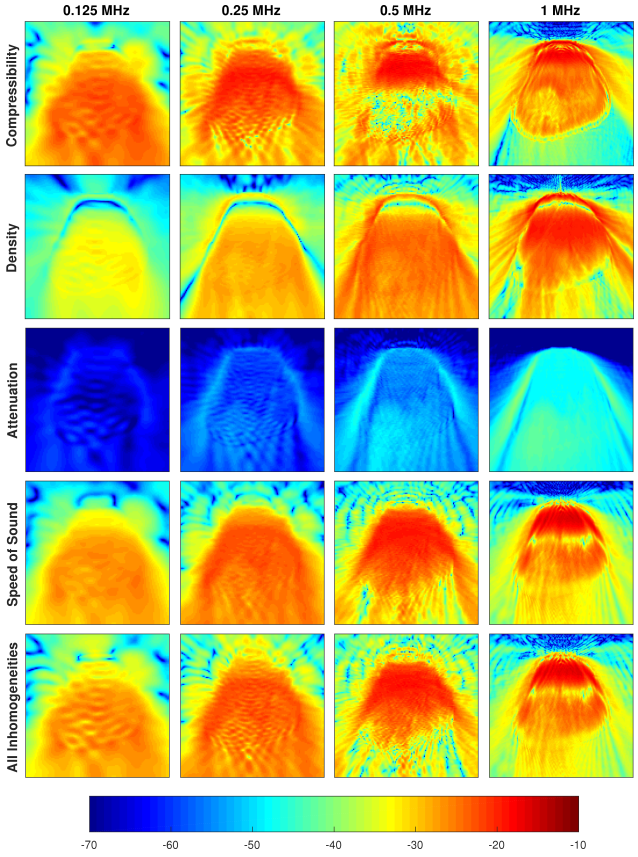

Fig. 3. Frequency-domain results for the scattered pressure field in the plane $z = 0$ m for different contrasts. The columns show results for different frequencies (from left to right 0.125 MHz, 0.25 MHz, 0.5 MHz, and 1 MHz); the rows for different contrasts (from top to bottom compressibility, density, attenuation, speed of sound and all inhomogeneities combined).

are given in the Table 3. The amount of scattering with inhomogeneities in attenuation is 24 dB less for 1 MHz and for other frequencies nearly 30 dB. Moreover, the results obtained with speed of sound case shows strong similarities with the all inhomogeneities combined case. Finally, the ripples visible inside the breast are spaced roughly one wavelength apart. They are caused by interference of the field inside the breast, and can be modeled via a full-wave method which allows for multiple scattering.

Table 3. Maximum values of the fields given in Fig. 3.

	0.125 MHz [dB]	0.25 MHz [dB]	0.5 MHz [dB]	1 MHz [dB]
Compressibility	−21.1	−18.6	−16.7	−14.6
Density	−31.1	−25.8	−20.4	−15.2
Attenuation	−58.1	−52.1	−46.1	−39.7
Speed of Sound	−24.4	−21.5	−18.5	−14.9
All Inhomogeneities	−23.4	−20.8	−17.8	−15.2

Next, time-domain wave fields are compared. Snapshots of the corresponding total wave fields for the five cases considered in Fig. 3 are displayed in Fig. 4. These time-domain results clearly show again that for low frequencies (e.g. 0.25 MHz), variations in attenuation become so small that there is almost no effect on the wave field. There is even no visible scattering, focusing or phase shift caused by attenuation at these frequencies. Finally, similarities in the results for the speed of sound and all inhomogeneities combined cases are again clearly visible.

4.3. Comparing the solution methods

Finally, results obtained with different solution methods are compared. The same breast model is used for every method; it only considers inhomogeneities in the speed of sound. For the remaining results, the wave field has a center frequency of $f_0 = 0.5$ MHz and is discretised using a time step $\Delta t = 0.5$ µs and a grid size $\Delta x = 0.39$ mm. Snapshots of the total field in the plane $z = 0$ m and at time $t = 65$ µs for one emitter are presented in Fig. 5.

With Born approximation, first order scattering is included in the model but phase shifts and multiple scattering are neglected. The total amount of scattering is clearly less than for the full-wave method which includes multiple scattering. The wavefront of the field propagates at the same speed as the incident field because of the lacking of additional phase shifts (caused by a spatially varying speed of sound) in the model.

The paraxial approximation provides more accurate results than the Born approximation; phase shifts, refraction and diffraction effects are clearly visible in the resulting wave field. The multiple scattering inside the breast shows similarities with the scattering modeled with the full-wave method. However, they are very different in the backward direction due to the approximation applied.

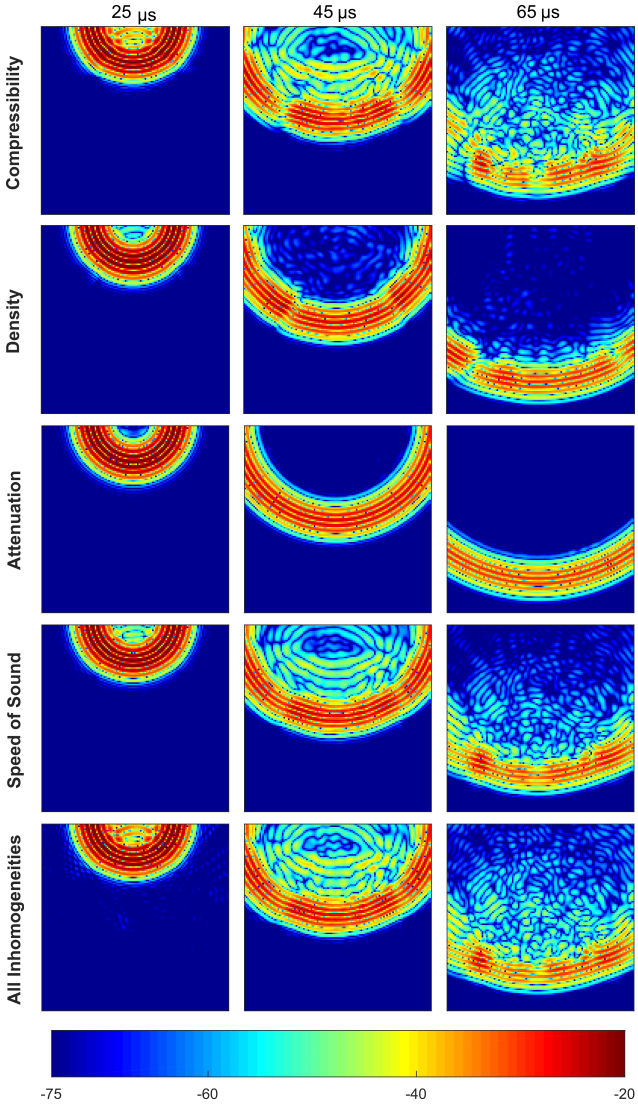

Fig. 4. Snapshots of the total wave field obtained within the full-wave method in the plane $z = 0$ m and at times $t = 25$ µs, 45 µs, 65 µs. The rows show the total fields obtained for different contrast functions (from top to bottom compressibility, density, attenuation, speed of sound and all inhomogeneities combined).

The ray based method clearly only considers phase shifts. Scattering, refraction, diffraction and attenuation effects are not taken into account with this method.

A-scans of the transmission and reflection measurements are shown in Fig. 6 and Fig. 7, respectively. All A-scans are normalized with respect to the maximum of the incident field and interpolated by zero padding in the frequency domain.

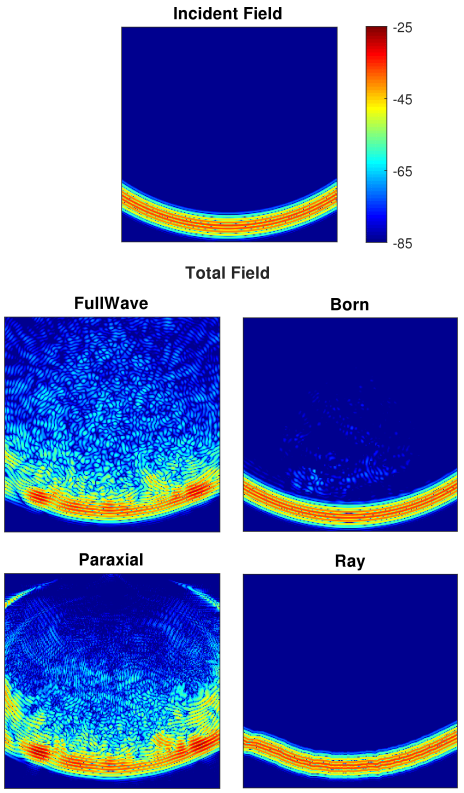

Fig. 5. Snapshots of the total wave field in the plane $z = 0$ m and at time $t = 65$ µs. Incident field placed at top and under that the total fields obtained for different methods (full-wave, parabolic, born, and ray).

The A-scan retrieved from the full-wave solution and measured below the breast deviates significantly from the remaining three solutions, see Fig. 6 left column. The A-scan obtained within the Born approximation shows an incorrect arrival of the wavefront and absence of scattering. For the paraxial solution the phase of the signal, especially for the waves arriving at a later time is erroneous. Although the arrival of the wavefront is modeled reasonably well with the ray based method, significant phase shifts do occur in the tail of the main wave field and multiple scattering is completely absent. Only the spectral profile of paraxial approximation shows small similarity with the spectral profile of the full-wave method.

The A-scans measured on the right-hand side of the breast are also shown in Fig. 6. The most noticeable artifacts for the A-scan obtained using the Born approximation are the incorrect amplitude of the wavefront and the absence of multiple scattering. Next, as expected due to its approximation, errors in the phase and amplitude of the field are visible in the results corresponding to the paraxial approximation, especially for the scattered waves arriving after the main wave field. This confirms that the paraxial approximation is only valid within a limited opening angle. Finally, the ray based method shows many similarities with the Born approximation, in particular the absence of multiple scattering and an incorrect amplitude of the wave field. The three measured spectral profiles correspon-

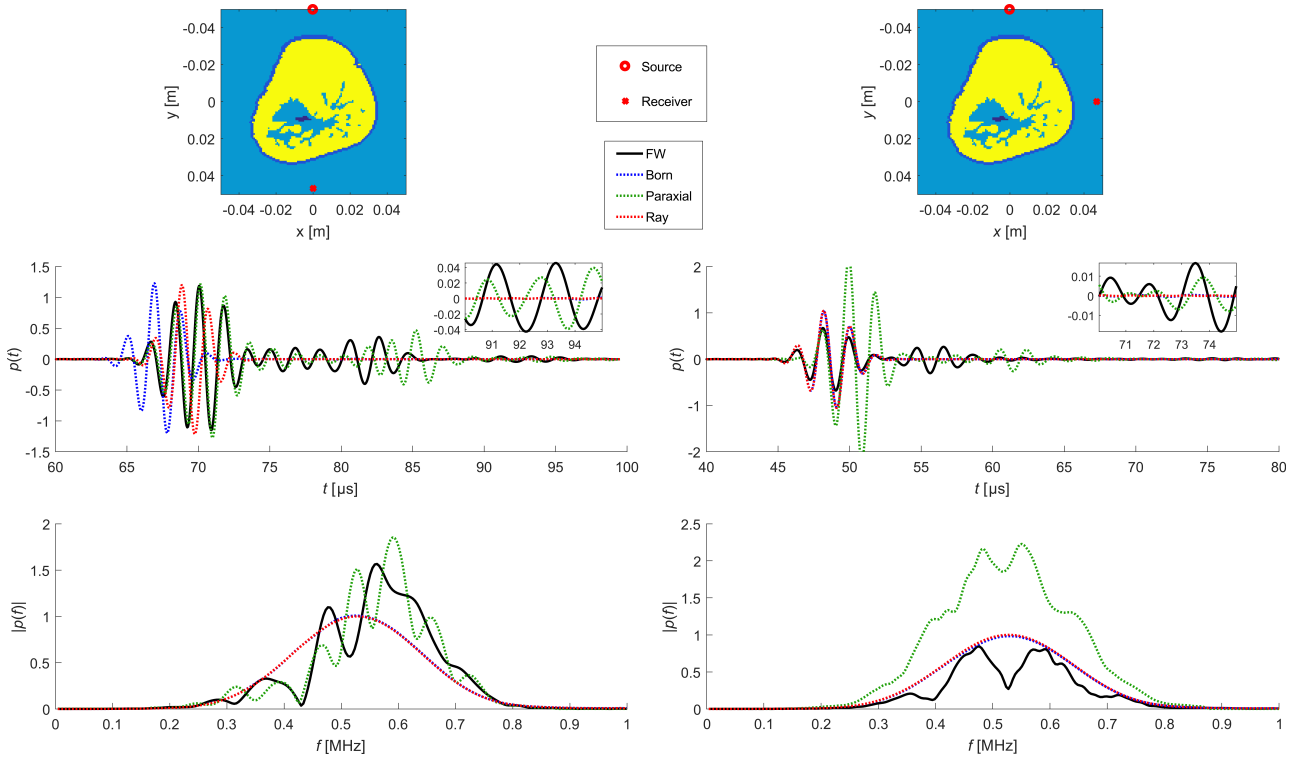

Fig. 6. A-scans for the transmission measurements. The A-scans are normalized with respect to the incident field. The top row shows the position of the source and the receiver, the middle row shows the time-domain results, and the bottom row shows the frequency-domain results.

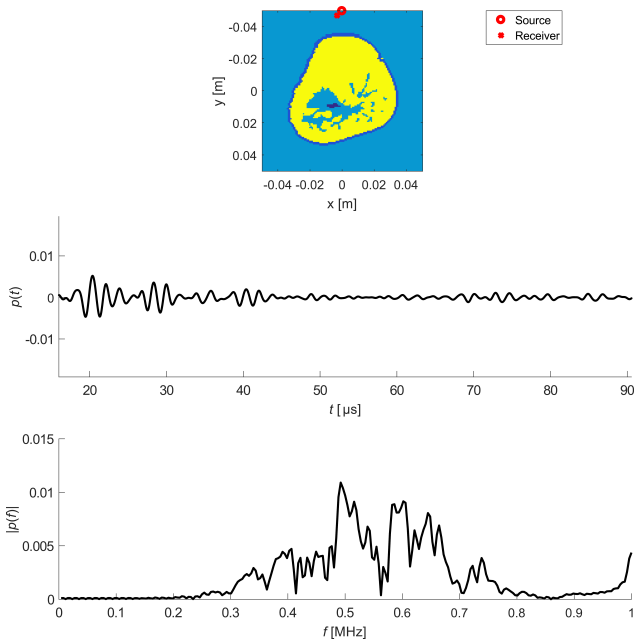

Fig. 7. A-scan for the reflection measurements using full-wave method. The A-scan is normalized with respect to the incident field. The top figure shows the position of the source and the receiver, the middle figure shows the time-domain result, and the bottom figure shows the frequency-domain result.

ding to the three approximations deviate significantly from the full-wave result.

The A-scan measured for the case when receiver is placed close to the source for retrieving the reflections are shown in Fig. 7. Straight ray and paraxial approximation in their basic form, which is used in this work, neglect backscattering. Since a comparison is not valid, the result of full-wave method is given only. Strong reflections at the beginning comes from the skin. Reflections that arrive later are mainly due to the inhomogeneities inside the breast.

5. Conclusion

A full-wave method based on a frequency-domain integral equation formulation is used to investigate to which extend spatial variations in the acoustic medium properties affect the acoustic pressure field in breasts. The same method is also used to validate the applicability of three solution methods commonly used to solve the forward problem for breast ultrasound.

The accuracy of the full-wave method, which is based on a frequency-domain integral-equation formulation, is confirmed using the analytical expression for a plane wave scattering off a soft spherical object. For the presented test with representative medium parameters, the error in the wave field is below −40 dB.

The effect of the heterogeneities belonging to the different medium properties are investigated separately and combined for the following frequencies: 0.125, 0.25, 0.5, and 1 MHz. The applied breast model is based on an MRI scan of cancerous breast and includes a spatially varying compressibility, density and attenuation. It is shown that the presented attenuation contrast causes significant less scattering (−24 dB) than the compressibility or density contrasts for frequencies below 1 MHz, suggesting that attenuation can be neglected for both the forward and inverse problem. The field scattering off the compressibility contrasts have a slightly higher amplitude than the field scattering off the density contrasts. Finally, the variations in the maximum amplitudes of the scattered fields corresponding to the speed of sound and all inhomogeneities included cases are 1 dB or less.

When comparing the excellent full-wave results with results obtained using the Born approximation, paraxial approximation and ray based method, it is shown that the latter approximations have serious shortcomings. In general, the main problem with the Born approximation is that it is lacking phase shifts and multiple scattering. The paraxial approximation is more accurate than the Born approximation as phase shifts and focusing effects are modeled. Unfortunately, the paraxial method is only valid within a limited opening angle and backscattering is not included. Therefore the paraxial approximation could only be used with good results for transmission tomography, but has in this regime an order of magnitude lower complexity than full wave approximation. The ray based method only considers phase shifts and neglects (back)scattering, refraction and diffraction effects. Consequently, the results from all three approximation methods are not accurate. This strongly limits its applicability for modeling breast ultrasound.

In conclusion, for frequencies below 1 MHz, scattering caused by attenuation can be neglected while both compressibility and density contrasts should be included in the model. In addition, considering only speed of sound variations in the medium is a valid approximation for these frequencies. Only the full-wave method yields accurate results, irrespective of the point of observation. The paraxial approximation may be considered as an alternative when the point of observation is located on the opposite side of the breast, as is the case for transmission tomography.

References

1. Alles E.J., van Dongen K.W.A. (2011), *Perfectly matched layers for frequency-domain integral equation acoustic scattering problems*, IEEE Transactions on Ultrasonics, Ferroelectrics and Frequency Control, **58**, 5, 1077–1086.

2. Bakker J.F., Paulides M.M., Obdeijn I., van Rhoon G.C., van Dongen K.W.A. (2009), *An ultrasound cylindrical phased-array for deep heating in the breast: theoretical design using heterogeneous models*, Physics in Medicine & Biology, **54**, 3201–3215.

3. Bird R.E., Wallace T.W., Yankaskas B.C. (1992), *Analysis of cancers missed at screening mammography*, Radiology, **184**, 3, 613–617.

4. Cobbold R.S.C. (2007), *Foundations of biomedical ultrasound*, Oxford University Press, New York.

5. Dagrau F., Rénier M., Marchiano R., Coulouvrat F. (2011), *Acoustic shock wave propagation in a heterogeneous medium: a numerical simulation beyond the parabolic approximation*, Journal of the Acoustical Society of America, **130**, 1, 20–32.

6. d'Astous F., Foster F. (1986), *Frequency dependence of ultrasound attenuation and backscatter in breast tissue*, Ultrasound in Medicine and Biology, **12**, 10, 795–808.

7. Demi L., van Dongen K.W.A., Verweij M.D. (2011), *A contrast source method for nonlinear acoustic wave fields in media with spatially inhomogeneous attenuation*, Journal of the Acoustical Society of America, **129**, 3, 1221–1230.

8. Duck F.A. (2013), *Physical properties of tissues: a comprehensive reference book*, Academic Press.

9. Duric N. *et al.* (2007), *Detection of breast cancer with ultrasound tomography: First results with the computerized ultrasound risk evaluation (C.U.R.E.)*, Medical Physics, **34**, 2, 773–785.

10. Fletcher R. (1976), *Conjugate gradient methods for indefinite systems*, [in:] *Numerical analysis*, pp. 73–89, Springer.

11. Fokkema J.T., van den Berg P.M. (1993), *Seismic Applications of Acoustic Reciprocity*, Elsevier, Amsterdam.

12. Gisolf A., Verschuur D.J. (2010), *The principles of quantitative acoustical imaging*, EAGE Publications, The Netherlands.

13. Goss S., Johnston R., Dunn F. (1980), *Compilation of empirical ultrasonic properties of mammalian tissues. II*, Journal of the Acoustical Society of America, **68**, 1, 93–108.

14. Hardin R., Tappert F. (1973), *Applications of the split-step Fourier method to the numerical solution of nonlinear and variable coefficient wave equations*, Siam Review, **15**, 423.

15. Herman G.C., van den Berg P.M. (1982), *A least-square iterative technique for solving time-domain scattering problems*, Journal of the Acoustical Society of America, **72**, 6, 1947–1953.

16. Hesse M.C., Schmitz G. (2012), *Comparison of linear and nonlinear unidirectional imaging approaches in ultrasound breast imaging*, Ultrasonics Symposium (IUS), 2012 IEEE International, pp. 1295–1298. IEEE.

17. Huijssen J., Verweij M.D., de Jong N. (2008), *Green's function method for modeling nonlinear three-dimensional pulsed acoustic fields in diagnostic ultrasound including tissue-like attenuation*, Ultrasonics Symposium (IUS), 2008 IEEE International, pp. 375–378.

18. Jirik R. *et al.* (2012), *Sound-speed image reconstruction in sparse-aperture 3-d ultrasound transmission tomography*, IEEE Transactions on Ultrasonics, Ferroelectrics and Frequency Control, **59**, 2, 254–264.

19. Kak A.C., Slaney M. (1988), *Principles of computerized tomographic imaging*, Vol. 33, SIAM.

20. Kleinman R.E., van den Berg P. M. (1991), *Iterative methods for solving integral equations*, Radio Science, **26**, 1, 175–181.

21. Ozmen N., Dapp R., Zapf M., Gemmeke H., Ruiter N.V., van Dongen K.W.A. (2015), *Comparing different ultrasound imaging methods for breast cancer detection*, IEEE Transactions on Ultrasonics, Ferroelectrics and Frequency Control, **62**, 4, 637–646.

22. Ozmen-Eryilmaz N., Demi L., Alles E.J., Verweij M.D., van Dongen K.W.A. (2011), *Modeling acoustic wave field propagation in 3D breast models*, Ultrasonics Symposium (IUS), 2011 IEEE International, pp. 1700–1703.

23. Ruiter N.V., Schwarzenberg G.F., Zapf M., Liu R., Stotzka R., Gemmeke H. (2006), *3D ultrasound computer tomography: Results with a clinical breast phantom*, Ultrasonics Symposium (IUS), 2006 IEEE.

24. Siegel R.L *et al.* (2017), *Colorectal cancer statistics*, CA: A Cancer Journal for Clinicians, **67**, 3, 177–193.

25. Simonetti F., Huang L., Duric N., Rama O. (2007), *Imaging beyond the Born approximation: An experimental investigation with an ultrasonic ring array*, Physical Review E: Statistical Physics, Plasmas, Fluids, and Related Interdisciplinary Topics, **76**, 3, 036601–036610.

26. Skudrzyk E. (2012), *The foundations of acoustics: basic mathematics and basic acoustics*, Springer Science & Business Media.

27. Sohrab B., Farzan G., Ashkan B., Amin J. (2006), *Ultrasound thermotherapy of breast: theoretical design of transducer and numerical simulation of procedure*, Japanese Journal of Applied Physics, **45**, 3R, 1856.

28. Stoffa P., Fokkema J.T., de Luna Freire R., Kessinger W. (1990), *Split-step Fourier migration*, Geophysics, **55**, 4, 410–421.

29. Szabo T.L. (1995), *Causal theories and data for acoustic attenuation obeying a frequency power law*, Journal of the Acoustical Society of America, **97**, 1, 14–24.

30. Szabo T.L. (2004), *Diagnostic ultrasound imaging: inside out*, Academic Press.

31. van Dongen K.W.A., Brennan C., Wright W.M. (2007), *Reduced forward operator for electromagnetic wave scattering problems*, IET Science, Measurement & Technology, **1**, 1, 57–62.

32. van Dongen K.W.A., Wright W.M.D. (2006), *A forward model and conjugate gradient inversion technique for low-frequency ultrasonic imaging*, Journal of the Acoustical Society of America, **120**, 4, 2086–2095.

33. Wiskin J., Borup D.T., Johnson S.A., Berggren M. (2012), *Non-linear inverse scattering: High resolution quantitative breast tissue tomography*, Journal of the Acoustical Society of America, **131**, 5, 3802–3813.

34. Zwamborn P., van den Berg P.M. (1992), *The three-dimensional weak form of the conjugate gradient FFT method for solving scattering problems*, IEEE Transactions on Microwave Theory and Techniques, **40**, 9, 1757–1766.